Earth and Planetary Science Letters 576 (2021) 117238

Contents lists available at ScienceDirect

Earth and Planetary Science Letters

www.elsevier.com/locate/epsl

Tectonic tremor as friction-induced inertial vibration

Kyungjae Im *, Jean-Philippe Avouac

Geology and Planetary Science Division, California Institute of Technology, Pasadena, CA 91125, United States

ARTICLE INFO

Article history:
Received 18 December 2020
Received in revised form 16 September 2021
Accepted 1 October 2021
Available online xxxx
Editor: R. Bendick

Keywords:
tremor
slow slip
low frequency earthquake
rate and state friction
inertial vibration

ABSTRACT

Slow slip events are often accompanied by tremor but how tremor is generated is yet elusive. In this study, we test the possibility that it is an inertial vibration. In the case of a single-degree-of-freedom spring and slider system with mass per unit area M, governed by rate-and-state friction with effective normal stress σ', excitation of inertial vibrations emerges when normal stress (σ') is low, and loading rate (V_l) is high. Accordingly, tremor can be excited in a low effective normal stress (σ') zone, for example, in a zone of high pore pressure, when the loading rate (V_l) is temporally increased, as can happen during a slow slip event. A high loading rate helps to sustain the vibration, but a long-lasting attenuating tremor can still be excited even with a moderate velocity perturbation as long as the normal stress is sufficiently small. We use numerical simulations to verify that this hypothesis holds for a one-dimensional fault. The dominant frequency of the tremor is close to the fundamental frequency of resonance of the frictionless shear crack at a low sliding rate. Higher frequency modes are excited at higher sliding velocity. We show simulations of spontaneous slow slip events associated with tremor radiated from inertial vibration of a fault patch with locally low effective normal stress. This model provides a possible explanation for tectonic tremor associated with slow slip events.

1. Introduction

Tremor, long-duration weak ground vibrations that lack the impulsive onset or seismic signal generated by regular earthquakes, have been observed in various geologic systems. Tremor can occur in volcanic and hydrothermal systems where it is generated at relatively shallow depth, typically less than 1-2 km, and is thought to be related to the presence of fluids (Julian, 1994; Chouet and Matoza, 2013). Similar signals originating from much greater depths, typically 40 km, were reported along subduction zones (Obara, 2002; Miller et al., 2002). There, tremor comes in association with transient slip events, commonly called slow slip events, which are detectable from geodetic measurements (Rodgers and Dragert, 2003; Schwartz and Rokosky, 2007; Beroza and Ide, 2011). Tectonic tremor along subduction zone is thought to be associated with zones of high pore fluid pressure (e.g., Shelly et al., 2006; Rubinstein et al., 2008; Hawthorne and Rubin, 2010; Brown et al., 2005; Audet and Schaeffer, 2018; Calvert et al., 2020). Tectonic tremor has also been observed on the San Andreas fault (e.g., Nadeau and Dolenc, 2005; Shelly, 2010; Rousset et al., 2019), where it also seems to be associated with high pore pressure (Thomas et al., 2012). Tremor is often interpreted as a swarm of low-frequency stick-slip events (e.g., Dmitrieva et al., 2013; Shelly et al., 2007; Luo and Liu, 2019). There is, however, no consensus view on how tremor is generated. Here we explore the possibility that it is due to inertial vibrations.

Friction-induced inertial vibrations are commonly observed in various mechanical systems, for example, in musical instruments (one can think of violin for example (e.g., Smith and Woodhouse, 2000)) and in vehicle brake systems (one can think of brake squeal for example (e.g., Kinkaid et al., 2003)). They are thought to arise from friction between sliding materials (Ibrahim, 1994). Modern friction laws recognize that friction depends on the slip rate and past history of sliding, generally using rate-and-state friction formalism (Marone, 1998). The rate-and-state friction is known to account well for the frictional behavior of various materials, rocks in particular (Baumberger and Caroli, 2006; Dieterich and Kilgore, 1994), as long as intense weakening mechanisms, such as flash heating, for example, are not activated. The rate-and-state friction law can lead to stable or unstable slip depending on the friction parameters (Rice and Ruina, 1983). Unstable slip arises from friction decreasing with sliding rate, and the slip motion (acceleration, deceleration, and arrest) is then controlled by inertia (Rice and Tse, 1986). Friction-induced vibration can arise in the case of an interface governed by rate-and-state friction when inertial influence is high (i.e., large mass, high slip velocity, and low normal stress) (Im et al., 2019).

---

* Corresponding author.
E-mail address: kjim@caltech.edu (K. Im).

https://doi.org/10.1016/j.epsl.2021.117238

In this study, we built on the analysis of Im et al. (2019) to show that inertial friction-induced vibrations can be excited by slow slip events on fault patches with high pore pressure. We first review the condition of tremor generation in the case of a simple, one-degree-of-freedom spring-and-slider system forced by a prescribed loading rate. Next, the analysis is expanded to a one-dimensional fault. Finally, we show simulations in which inertial vibrations are generated during spontaneous slow slip events by a fault patch with locally low effective normal stress.

2. Frictional stability and inertial vibrations with rate-and-state friction

Here, we first review the condition of frictional stability and inertial vibration in the case of a single-degree-of-freedom spring-slider system obeying rate-and-state friction (RSF) (Im et al., 2019). Next, we review the stability analysis of one-dimensional fault anti-plane slip (Rice et al., 2001) and compare the two stability conditions.

2.1. Spring and slider system

In the RSF framework, friction is dependent on slip velocity and a state variable θ (Dieterich, 1979; Ruina, 1983). We use the most common RSF law,

$$\mu = \mu_0 + a \ln\left(\frac{V}{V_0}\right) + b \ln\left(\frac{V_0\theta}{D_c}\right), \tag{1}$$

where μ_0 is a reference friction coefficient at reference velocity V_0, D_c is a critical slip distance, and a and b are empirical constants for the magnitude of direct and evolution effects, respectively.

Different formulations have been proposed to describe the state variable (θ) evolution. In this work, we use the 'slip' law (Ruina, 1983), which provides the best match to laboratory observations (Bhattacharya et al., 2015),

$$\frac{d\theta}{dt} = -\frac{V\theta}{D_c} \ln\left(\frac{V\theta}{D_c}\right). \tag{2}$$

However, the analysis presented here also applies to the other commonly used evolution law, the 'aging law' (Dieterich, 1979), as shown by Im et al. (2019).

The equation of motion of the spring and slider system is

$$M\ddot{\delta} = K(\delta_l - \delta) - \mu\sigma', \tag{3}$$

where M is mass per unit area (kg/m^2), K is a stiffness expressed in units of shear stress (Pa/m), σ' is effective normal stress, δ_l is load point displacement, and δ is slider displacement.

Assuming that the friction parameters (a, b, D_c) are constant, sliding at velocity V_l can be stable only when $K > K_c$ where the critical stiffness K_c is (Rice and Ruina, 1983),

$$K_c = \frac{(b-a)\sigma'}{D_c}\left[1 + \frac{MV_l^2}{\sigma' a D_c}\right]. \tag{4}$$

The critical stiffness can thus be written as the sum of a quasistatic critical stiffness,

$$K_{c,qs} = \frac{(b-a)\sigma'}{D_c}, \tag{5}$$

and of a dynamic critical stiffness,

$$K_{c,dyn} = \frac{b-a}{a}\frac{MV_l^2}{D_c^2}. \tag{6}$$

The second term in the bracket of equation (4) is a dimensionless number that quantifies the contribution of inertia to frictional instability,

$$\eta = K_{c,dyn}/K_{c,qs} = \frac{MV_l^2}{\sigma' a D_c}. \tag{7}$$

This term implies that the system tends to become unstable for a larger mass or velocity. Since this term is sensitive to loading velocity ($\eta \sim V_l^2$), any velocity weakening ($a - b < 0$) system can become unstable at sufficiently high velocity. We also introduce a dimensionless critical stiffness,

$$\kappa_c = \frac{K_c}{K}. \tag{8}$$

The two dimensionless parameters κ_c and η determine if the system yields stick-slip motion or stable sliding and inertial vibrations or not. The slip is unstable if $\kappa_c > 1$ (Rice and Ruina, 1983). Im et al. (2019) showed that the inertial vibration tends to emerge when $\eta > 1$. We note that $\kappa_c = 1$ is a strict linear stability criterion as, mathematically, it defines a Hopf bifurcation point, but $\eta = 1$ is not. Im et al. (2019) showed that the emergence of inertial vibration is also influenced by K. Equation (7) implies that the harmonic inertial vibrations may emerge when the inertial term, MV_l^2, is high or normal stress is low.

Fig. 1 shows how the sliding mode of the spring-and-slider system varies depending on the loading velocity (V_l) and effective normal stress (σ'). Since κ_c and η are dependent on the normal stress and loading velocity, the V_l – σ' space can be divided into four different zones (Fig. 1a): (i) $\kappa_c > 1$ & $\eta < 1$ (unstable & low-inertia) where sliding is stick-slip (Figs. 1b&c); (ii) $\kappa_c > 1$ & $\eta > 1$ (unstable & high-inertia) where sliding results in quasi-harmonic vibrations (Figs. 1d,g&j); (iii) $\kappa_c < 1$ & $\eta < 1$ (stable & low-inertia) where sliding rapidly converges to stable sliding (Figs. 1e&h); (iv) $\kappa_c < 1$ & $\eta > 1$ (stable & high-inertia) where harmonic vibration attenuates until stable sliding is established (Figs. 1f&i).

We see that although the vibration emergence criterion is not rigorously derived, it does approximatively capture the condition for the emergence of inertial vibrations in our numerical simulations. Tremor can actually occur as an attenuating vibration even if $\kappa_c < 1$. This observation considerably broadens the condition for tremor generation since it significantly reduces the velocity requirement. For example, if the condition of $\kappa_c > 1$ were essential for tremor generation, high-velocity loading (>~1 mm/s in Fig. 1a) would be required to generate tremor. However, thanks to inertia, if normal stress is sufficiently low, long-lasting vibrations can occur with a moderately perturbed loading rate (e.g., Fig. 1i) by, for example, a nearby slow slip event. Fig. 1h exhibits subtle vibration even at ($\eta < 1$), implying that the domain where vibration can emerge is broader and not strictly delimited by $\eta = 1$. This mechanism could explain tectonic tremor, which is thought to occur where pore pressure is near lithostatic (e.g., Shelly et al., 2006; Rubinstein et al., 2008; Hawthorne and Rubin, 2010) and in association with slow slip events, typically a few orders of magnitude larger than the tectonic loading rate.

The inertial vibrations generated by single-degree-of-freedom spring and slider system are harmonic, as can be seen in Fig. 1, with a frequency close to the fundamental frequency of the mass-spring system (Im et al., 2019):

$$f_n = (1/2\pi)\sqrt{K/M}. \tag{9}$$

Note that the vibration frequency is independent of the loading velocity. Given the simulation parameters $K = 40$ MPa/m and $M = 450000$ kg/m^2, the fundamental frequency is ~ 1.5 Hz, which is close to the dominant frequency observed in the simulations that show inertial vibrations (panels (d), (f), (g), (i), and (j) of Fig. 1).

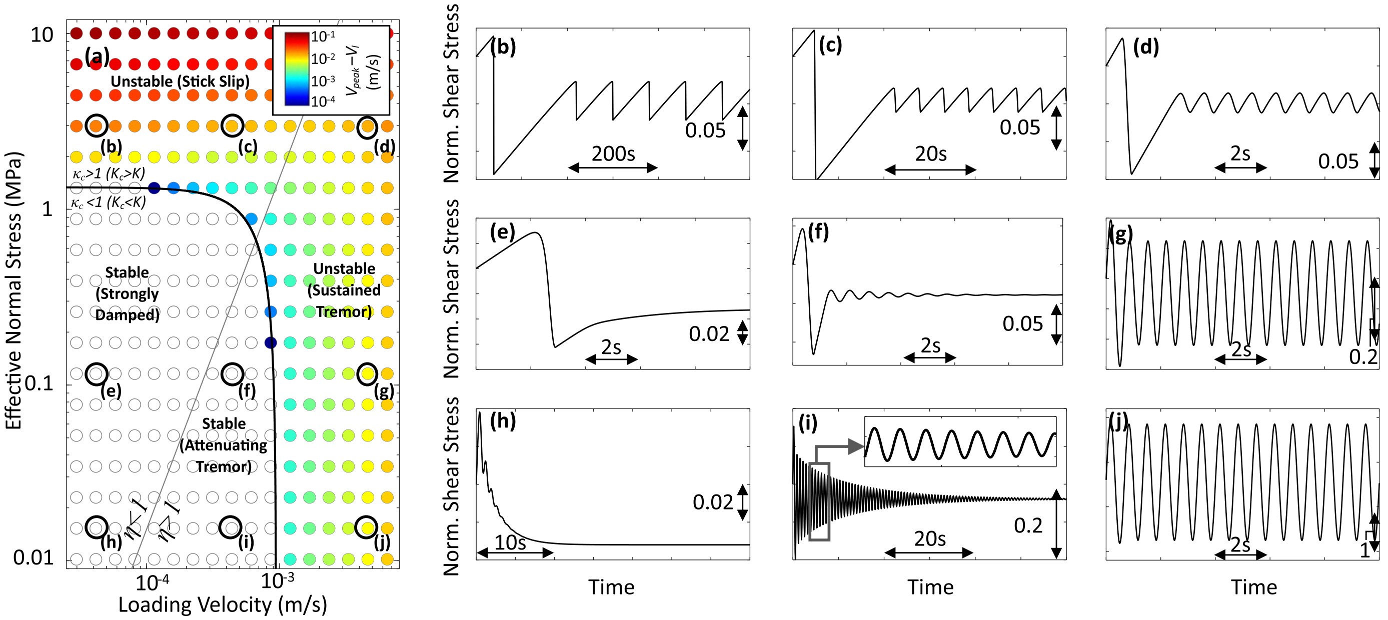

Fig. 1. Synoptic view of the behavior of the spring-and-slider system. (a) Peak velocity. Empty gray circles denote stable sliding. Curved black line denotes theoretical stability transition, $\kappa_c = 1$, and gray line denotes $\eta = 1$. (b-j): normalized (divided by normal stress) shear stress curves of selected (marked in panel a) cases. We used rate-and-state parameter $a = 0.003$, $b = 0.006$, $D_c = 100$ µm, $M = 450000$ kg/m^2, $K = 40$ MPa/s and initial velocity 1 nm/s. The mass M represents ~190 m height rock mass with a density of 2400 kg/m^3. This value was tuned to match the dynamic simulations of Fig. 4 (~1.5 Hz vibration in ~1 km fault patch). The stiffness is equivalent to a 1 km long fault with shear modulus G = 30 GPa and Poisson ratio 0.25 (Equation (12)).

2.2. Stability of one-dimensional fault slip

The linear stability analysis of a one-dimensional fault with rate and state friction was conducted by Rice et al. (2001). They define a critical wavenumber from anti-plane velocity perturbation. The critical wavelength λ_c is twice the critical fault length L_c, so the critical wavenumber is $k_c = 2\pi/\lambda_c = \pi/L_c$. The linear stability condition presented by Rice et al. (2001) can then be written

$$K_c \approx \frac{G}{L_c} = \frac{2}{\pi}\frac{(b-a)\sigma'}{D_c}\sqrt{1+q^2}, \tag{10}$$

where

$$q = \frac{GV_l}{2\sqrt{a(b-a)}\sigma' c_s}, \tag{11}$$

G is shear modulus, and c_s is shear wave speed. The dimensionless number q defines the contribution of dynamic effect to frictional instability. Similar to η, q increases at high velocity and low normal stress. The first expression $K_c \approx G/L_c$ in equation (10) comes from the equivalent lumped stiffness typically introduced to estimate the stiffness of a one-dimensional fault (Dieterich, 1992):

$$K = \frac{\alpha G}{L}, \tag{12}$$

where α is a shape factor, typically close to 1, and L is the length of the unstable fault patch.

The stability criterion for the spring-slider system (equations (4)) and 1D fault (equations (10) and (11)) can be compared by the equivalent stiffness of slipping patch $K \approx G/L$. It is apparent that equations (10) and (4) are comparable at the quasistatic limit ($\eta \ll 1$ and $q \ll 1$). One can further show that equations (10) and (11) are equivalent to equation (4) at the dynamic limit ($\eta \gg 1$ and $q \gg 1$) as well. Substituting $c_s = \sqrt{G/\rho}$ and equation (11) into (10) with assuming dynamic limit $q \gg 1$, equation (10) can be rewritten as

$$K_{c,dyn} \approx \frac{G}{L_c} = \frac{b-a}{a}\frac{V^2}{D_c^2}\frac{\rho L_c}{\pi^2}. \tag{13}$$

Equation (13) is equivalent to dynamic critical stability of the spring slider system (i.e., equation (6)) when the lumped mass per unit area M is

$$M \approx \frac{\rho L}{\pi^2}. \tag{14}$$

The notion of a lumped mass, in addition to the equivalent stiffness (equation (10)), makes it possible to represent approximatively the behavior of finite size fault with account for inertial effects. We verify below the correspondence and calibrate the lumped mass in our numerical simulations of inertial vibration of a 1D fault (equation (21)).

3. Simulation methods

We use two different methods to simulate frictional sliding along a one-dimensional fault with inertia. First, we conduct fully dynamic finite difference simulations taking into account inertia and the dynamic stresses associated with the elastic wave propagation in the medium. Because of the computational cost and some numerical instabilities we observed at extremely low normal stress cases with this method, we use this simulation method to validate the emergence of inertial vibration at moderately low normal stress (1 MPa) and to calibrate the simulations done with the other method. Alternatively, we use a lumped-mass boundary element method to systematically explore how the vibration evolves depending on the loading rate and effective normal stress. We also use this method to test if inertial vibrations can arise on a patch with locally low effective normal stress embedded in a fault that can produce spontaneous slow slip events.

3.1. Fully dynamic finite difference simulations

We used FLAC 3D (Itasca Consulting Group Inc., 2007) to simulate the fully dynamic response of a large domain bounded by a

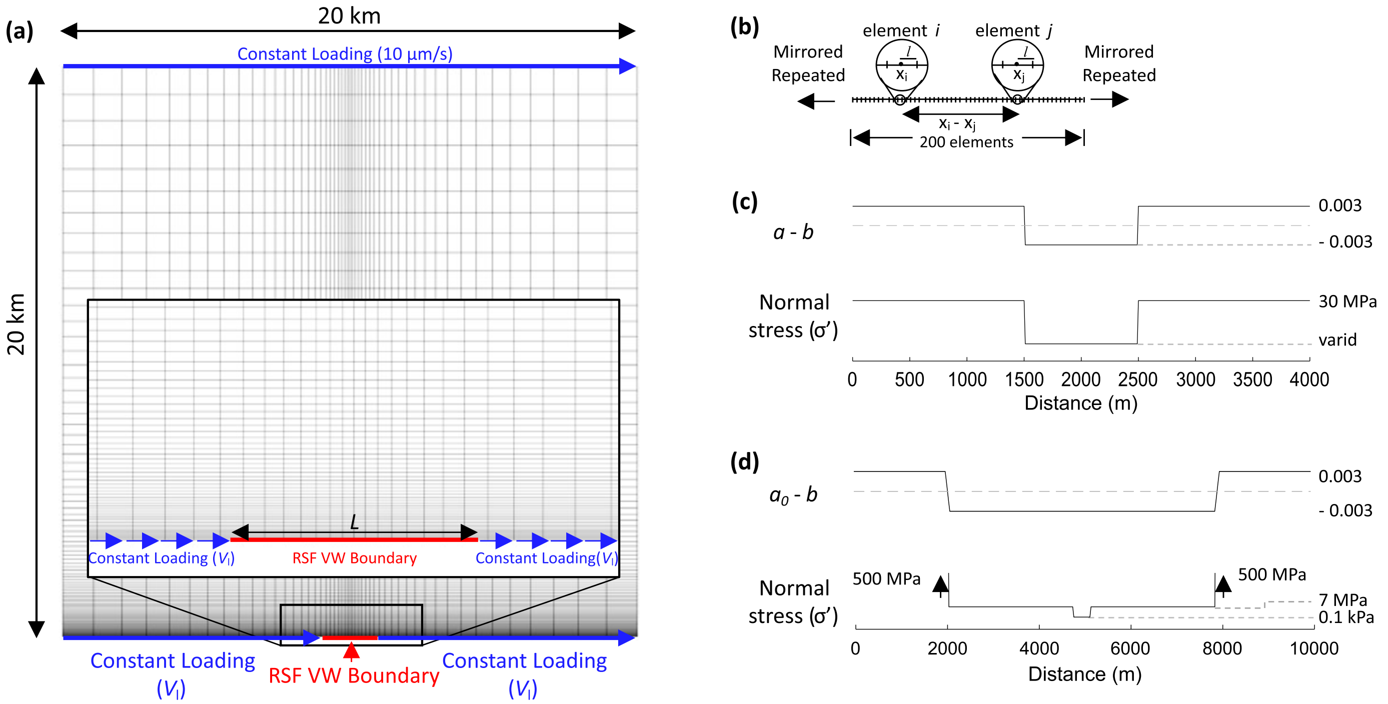

Fig. 2. Simulation Methods. (a): Finite difference simulation domain. Normal stress 1 MPa, density 2400 kg/m^3 is assigned to 20 km × 20 km 2D plane strain rock mass. The bottom boundary is divided into constant loading (blue arrows) and velocity weakening RSF boundary of length L (red line). See supplementary materials for more detail. (b): Illustration of boundary elements. The quasistatic displacement-stress relationship between two boundary elements in panel b is defined in equation (16). (c, d): Simulation parameters for constant loading rate (c) and slow slip (d) boundary element simulations. Actual simulation is conducted in half of the simulation domain. (For interpretation of the colors in the figure(s), the reader is referred to the web version of this article.)

shear fault and assuming plane strain. The overall domain size is set to 20 km × 20 km, which is large enough to avoid influence from wave reflection at the boundaries. The intent is to simulate the response of the rate-weakening fault patch (red line in Fig. 2a) to the loading resulting from a slow slip event on the surrounding fault area (blue arrows in Fig. 2a). The loading rate is constant. So, these simulations ignore that the dynamics of the slow slip event might be affected by the response of the RSF fault patch.

We conducted simulations with 6 different fault lengths ($L =$ 693, 942, 1218, 1526, 1867, 2246 m) with shear modulus $G =$ 30 GPa and rock density $\rho = 2400$ kg/m^3. To define the influence of rock modulus and density, we additionally conducted simulations with two different $G - \rho$ combinations: (i) $G = 15$ GPa and $\rho = 2400$ kg/m^3 and (ii) $G = 30$ GPa and $\rho = 500$ kg. Normal stress is 1 MPa in the entire domain and loading rates V_l are varied within the range of $0.1 \sim 1$ mm/s to define the influence of velocity on the transition from stick-slip to vibration. For the velocity weakening fault patch, we assigned rate and state friction parameters $a = 0.003$, $b = 0.006$, and $D_c = 20$ μm (see supplementary material and figure S1 for more details).

3.2. Lumped mass boundary element

In the boundary element simulations, the system is simplified via two assumptions: (i) stress transfer is assumed quasistatic, and (ii) mass is lumped at each boundary element. Hence, the simulation is computationally much lower-cost and allows for small timestep and element size. We use this simulation method to explore how a rate-weakening RSF fault patch responds to forcing by an imposed slip rate and might generate tremor. These simulations are designed to be comparable to those run with FLAC. The parameters are tuned to yield matching results. We also use this simulation approach to simulate the coupling between spontaneous slip events and tremor generating fault patches.

We set a mirrored-and-repeated one-dimensional boundary element fault surface in an infinite medium (Fig. 2b). Frictional properties and normal stresses are heterogeneous (Fig. 2c&d). With the simplifications above, the momentum balance equation at i^{th} boundary element is

$$M_i\ddot{\delta}_i = \sum_j K_{ij}(V_{loading}t - \delta_j(t)) - \mu_i\sigma_i', \qquad (15)$$

where M is lumped mass per unit contact area of each element, δ is displacement, $V_{loading}$ is far-field loading velocity, t is time, μ is friction, σ' is effective normal stress, and K_{ij} is a stiffness matrix that defines the elastic stress change at element i from the displacement of element j. The left-hand side term is a direct calculation of the inertia effect from lumped mass M_i. The first term on the right-hand side represents the sum of all the applied stress to the ith element by the displacements of jth elements and far-field loading. And the last term represents frictional resistance.

Our formulation (equation (15)) differs from the boundary element approximation in which the effect of inertia is accounted for with radiation damping (Rice, 1993). Instead of the mass × acceleration in equation (15), radiation damping approximates inertia by velocity-dependent damping, representing energy radiation as seismic waves (Rice, 1993). Our lumped mass approximation does not consider the energy radiation effect and possibly overestimates the inertia effect. We choose the lumped mass approximation because the stability of 1D fault dynamical behavior (equation (13)) is comparable to the spring-slider system (equation (17)). In contrast, the radiation damping approximation does not allow for comparison with the linear stability analysis. For example, stability analysis in 1D fault slip (equation (10) and (11)) shows that the fault slip becomes unstable at a high velocity. However, the radiation damping approximation results in slip being stabilized as velocity increases (e.g., Dmitrieva et al., 2013). We could have alternatively used a boundary integral method, which allows fully dynamic sim-

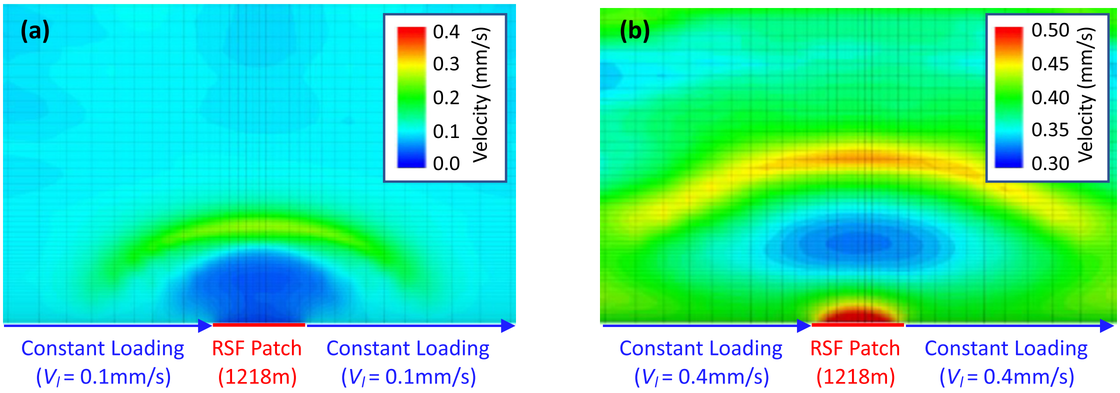

Fig. 3. A snapshot of velocity field for (a) stick-slip motion ($V_l = 0.1$ mm/s; Fig. 4 black line) and (b) harmonic vibration ($V_l = 0.4$ mm/s; Fig. 4 red line). Simulated RSF fault patch is 1218 m. (see also supplementary videos S1 and S2).

ulations (Lapusta et al., 2000). We opted for the lumped mass model for consistency with our previous contributions on the modeling of slow slip events (Im et al., 2020) and inertial vibrations (Im et al., 2019).

The mass per unit area M can be rewritten as $M = \rho h_c$, where ρ is rock density and h_c is the characteristic height of the rock mass (vertical from contact area), which defines the vertical range of inertial influence. The parameter h_c (and therefore M as we assume uniform ρ) is independent of the simulation element size but depends on the fault length. Below, we show that M (*and hence*, h_c) and the fault length L are linearly dependent (equation (21)) for the frequency of the 1st inertial vibration mode to be equivalent in the two types of simulations, as also derived from the stability analysis (equation (14)). The value of M in the boundary element simulations is selected based on this criterion.

Since we assume quasistatic stress transfer, K_{ij} can be written as (Crouch, 1976; Dieterich, 1992):

$$K_{ij} = \frac{G}{2\pi(1-\nu)}\left(\frac{1}{x_i - x_j + l} - \frac{1}{x_i - x_j - l}\right), \tag{16}$$

where G is the shear modulus, ν is the Poisson coefficient, and l is the half-length of the element.

We solve Equation (15) with the method of Im et al. (2017), which ensures numerical stability. To apply the spring-slider solver, we rewrite equation (15) into a spring-slider form (i.e., equation (3)),

$$M_i\ddot{\delta}_i = K_{ii}(\Lambda_i - \delta_i) - \mu_i\sigma_i', \tag{17}$$

where the loading from the surrounding fault displacement at ith node Λ_i is

$$\Lambda_i = V_{loading}t + \sum_{j\neq i}\frac{K_{ij}}{K_{ii}}\left(V_{loading}t - \delta_j\right). \tag{18}$$

3.2.1. Constant loading rate

We simulate a 4 km mirrored-repeated fault in a medium with $G = 30$ GPa and $\nu = 0.25$. The rate-weakening fault patch is 1 km long with RSF parameters: $a = 0.003$, $b = 0.006$. The surrounding fault has constant normal stress (30 MPa) and is velocity strengthening with RSF parameters: $a = 0.006$, $b = 0.003$ (Fig. 2c). For comparison with Fig. 1, we explore a range of effective normal stress on the velocity-weakening fault patch and loading velocity. The velocity strengthening zone is initialized with a steady-state at a given initial velocity. The velocity weakening zone is initialized with 1/10 of the loading rate to apply initial stress perturbation. We assigned $M_i = 450000$ kg/m^2 to each element, a value that was determined to yield frequency similar to those obtained in the fully dynamic finite difference simulation result (1.5 Hz at $L \sim 1000$ m).

3.2.2. Slow slip and inertial vibrations

The difference with the previous simulations is that the fault is assigned a friction law that allows for spontaneous SSEs. This is achieved by a transition from rate-weakening behavior at a low sliding rate, so that instabilities can emerge, to rate-strengthening at a higher sliding rate, so that the slip rate can't reach values typical of seismic slip (Rabinowitz et al., 2018; Im et al., 2020). The point of the simulation is to test if a zone with high pore pressure anomaly (low normal effective stress) within the source of slow slip events may produce inertial vibrations due to the temporary increased loading rate.

The fault length is 10 km and is loaded at tectonic loading rate ($V_l = 0.5$ nm/s). The fault is divided into (i) a high normal stress (500 MPa) stable sliding ($a_0 - b > 0$) zone, (ii) a low normal stress (7 MPa) slow earthquake zone ($a_0 - b < 0$) and, additionally, (iii) a central slow earthquake zone ($a_0 - b < 0$) with extreme lower normal stress (0.1 kPa) (Fig. 2d). We assumed localized high-pressure zone (400 m) imbedded in relatively large (5.6 km) slow slip zone. Since the expected inertial vibration fault length is shorter (400 m) than in the previous simulations (1 km), we use smaller mass per unit area ($M = 180000$; equation (21)).

The friction parameters at low velocity are identical to those chosen in the other simulations ($a_0 = 0.003$, $b = 0.006$ for unstable, $a_0 = 0.006$, $b = 0.003$ for stable), but 'a' is now velocity dependent according to:

$$a(V) = a_0 + S_a\log_{10}\frac{V_a + V}{V_a}. \tag{19}$$

We used $V_a = 2\times10^{-8}$ m/s and $S_a = 0.001$/decade. These values are consistent with laboratory experiments and can produce realistic slow slip events (Im et al., 2020).

4. Simulation results

4.1. Finite difference simulations

All simulation results show unstable sliding as expected from the stability analysis. With our input parameter of finite difference simulations (G = 30 GPa, $\nu = 0.25$, $b - a = 0.003$, $\sigma' = 1$ MPa, $D_c = 20$ μm with $\alpha = 1$), the quasistatic ($V = 0$) critical length $L_c \sim 314$ m (equation (10)), which is smaller than the shortest fault length tested (693 m). At a slow loading rate, the central RSF patch produces repeating stick-slip instabilities (Fig. 3a, Fig. 4 black lines). When the loading rate is higher, it produces quasi-harmonic vibrations as the high loading rate limits the possibility

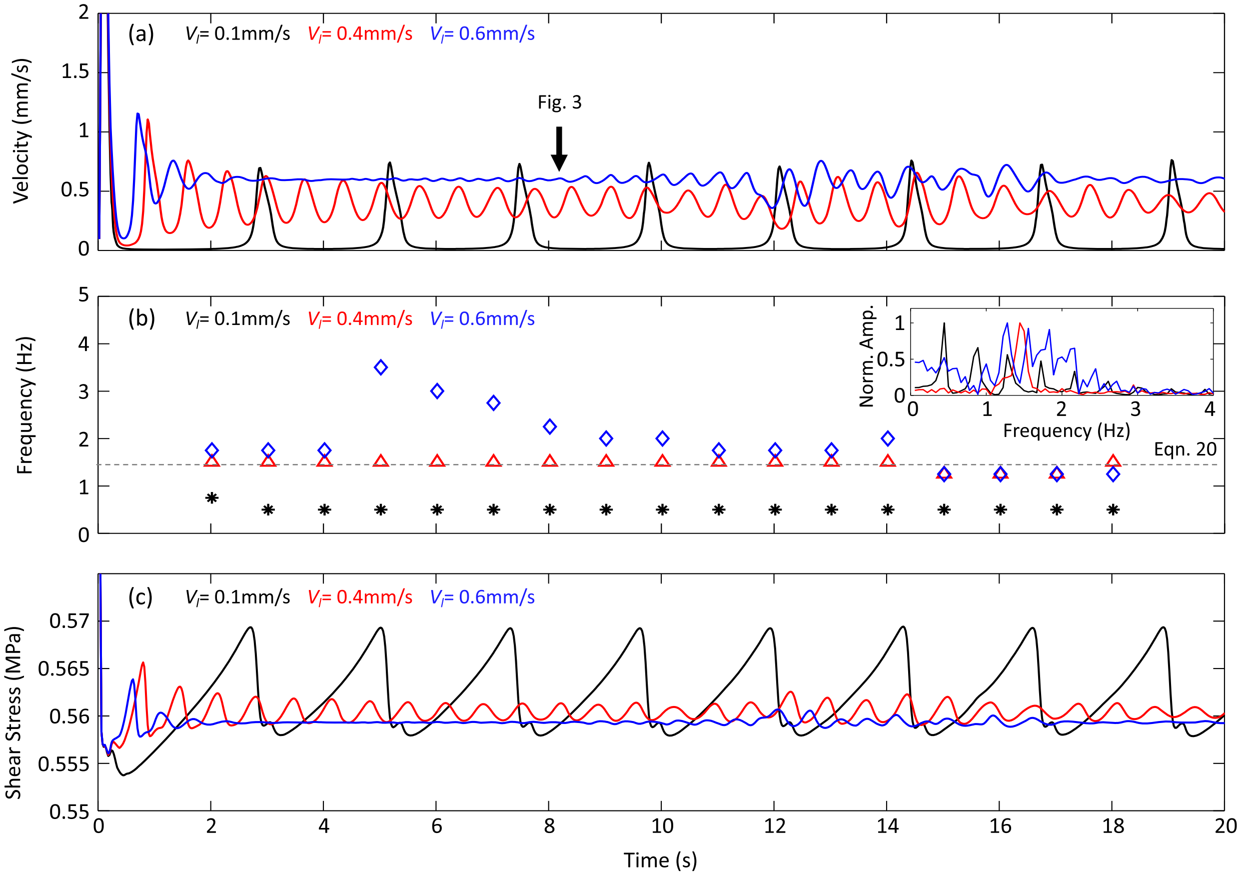

Fig. 4. Velocity (a), frequency (b) and shear stress (c) evolution with time at the center of the RSF patch with unstable patch size $L = 1218$ m and shear modulus $G = 30$ GPa (see figure S6-S23 for different patch size $L = 693$, 942, 1526, 1867, 2246 m, density $\rho = 500$ kg/m^3 and shear modulus $G = 15$ GPa cases). The different symbols in (b) represent the frequency of highest amplitude harmonic vibrations calculated within 4 s (-2 s to $+2$ s from the plotted point) moving time window. Curves and symbols are colored according to the loading rate. The dashed horizontal line denotes the frequency of the 1st mode of inertial vibration calculated with equation (20). Inset in panel b shows normalized amplitude spectra (1-20 s).

for the quasistatic low-velocity stage that would occur between stick-slip events (Fig. 3b, Fig. 4 red and blue lines). When the motion is stick-slip, a single propagating wave is apparent (Fig. 3a). During inertial vibrations, the velocity field shows radiated harmonic waves (Fig. 3b) (see also supplementary video S1 and S2).

For the loading velocity of 0.1 mm/s with $L = 1218$ m, the model yields periodic stick-slip events with a frequency of ~0.5 Hz, dictated by the ratio of the stressing rate to the co-seismic stress drop (Fig. 4c). When the loading velocity is 0.4 mm/s, the model yields inertial quasi-harmonic vibrations with a frequency of ~1.5 Hz (Fig. 4b inset). We observe that the periodicity of the vibrations breaks up at a higher velocity of 0.6 mm/s (Fig. 4b inset). In this case, the dominant frequency evolves with time (blue markers around 5-8 s in Fig. 4b). This drift would not happen with a spring-and-slider system, in which a velocity increase only results in a larger amplitude of the harmonic vibrations (Im et al., 2019). A difference between the spring-and-slider and the one-dimensional fault simulations is that the finite-size fault does not always yield a single mode of fault vibration (e.g., Fig. 6). The temporal high-frequency drifts down and seems to be stabilized around ~1.5 Hz, which roughly corresponds to the frequency of the periodic harmonic vibration (red triangles in Fig. 4b).

We find that the frequency of the inertial vibration in 1D fault can be estimated by assuming that it arises from a resonance whereby the fault length is half the wavelength of the shear wave:

$$f_n = 1/2L\sqrt{G/\rho}, \qquad (20)$$

where L is fault length, G is shear modulus, and ρ is the density of the rock. Using the parameters corresponding to the simulations of the figure ($G = 30$ GPa, $\rho = 2400$ kg/m^3), the fundamental frequency for $L = 1218$ m is 1.45 Hz (dashed line in Fig. 4b), which matches the frequency of harmonic vibrations.

The transition from stick-slip to inertial vibrations and the frequency of the inertial vibrations should be dependent on rock density. We, therefore, ran simulations with different densities (figure S2). The lower density simulation is similar to the higher density case in the stick-slip regime but with a higher peak slip rate and shorter event duration (figure S2a). At velocity $V_l = 0.4$ mm/s, the lower density case is still in the stick-slip regime, but the higher density case is in the inertial vibration regime (figure S2b). The low-density case results in inertial vibration at $V_l = 0.8$ mm/s (figure S2c), with frequency of ~ 3 Hz, which is ×2 larger than high-density case, and is close to the estimated value of 3.18 Hz based on equation (20) ($G = 30$ GPa, $\rho = 500$ kg/m^3) (figure S20).

The theoretical frequency expressed by equation (20) is further verified by varying the fault length and shear modulus (Fig. 5). The frequencies of the vibrations observed in the simulation (black markers) match well the predicted values (red lines). The frequencies corresponding to the fundamental mode (mode 1) generally increase with velocity. Furthermore, we see that higher modes are excited at high velocity ($V_l = 6 \times 10^{-4}$) for long fault patches ($L > 1500$) in the lower shear modulus case (Fig. 5b). These frequencies correspond to the second and third harmonics of the fundamental mode, as seen in Figs. 5 and 6. In the higher modes, the fault length is equal to multiples of the half wavelength of the

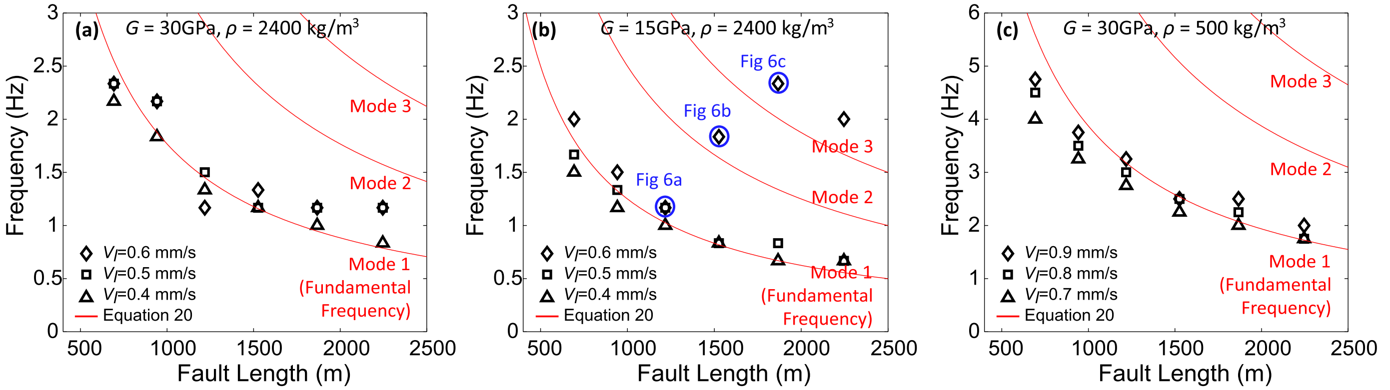

Fig. 5. Frequency of inertial vibration simulation results. Stick-slip results are excluded. See Figure S6-S23 for the entire simulation results. Red lines denote equation (20) (mode 1) and its multiples (×2 for mode 2 and ×3 for mode 3). The frequencies are calculated from velocity curves between 13-19 s. The higher mode vibrations shown at a high loading rate in softer medium (blue circles in b) are presented in Fig. 6.

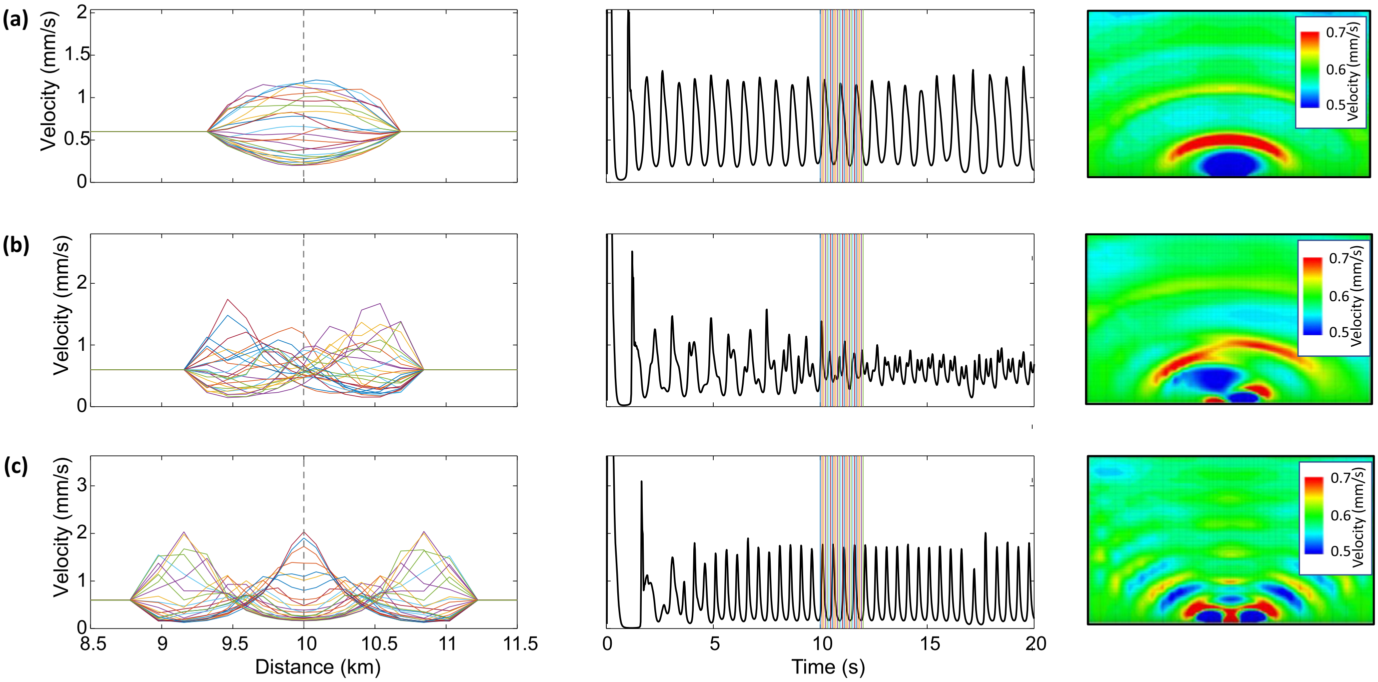

Fig. 6. Mode 1 (a), mode 2 (b) and mode 3 (c) inertial vibrations. The simulation parameters for each case are denoted in Fig. 5 (Fig. 5b blue circles). Left panels show spatial evolution, middle panels show temporal evolutions at the central fault patch (at 10 km in the left panels), and right panels show snapshots of the velocity field for the vibrations (see also supplementary videos S3-S5). We tested simulation (c) with finer grid size to test grid size effect on high mode vibration development and obtained nearly identical results (figure S3).

shear waves patch (i.e., ×2 and ×3) (Fig. 5 mode 2 and 3 red lines, Fig. 6).

We can derive the equivalent mass per unit area M for the inertial vibration simply by equating the two expressions for the fundamental frequency (equations (9) and (20)). Given the expression for the equivalent stiffness K (equation (12)), we get:

$$M = \frac{\alpha \rho L}{\pi^2} \tag{21}$$

This is essentially identical to the lumped mass expression derived from the 1D stability analysis (equation (14)).

4.2. Boundary element simulations

4.2.1. Influence of normal stress and loading rate

We use the boundary element method to conduct simulations at various normal stresses and loading rates spanning the $\kappa_c = 1$ and $\eta = 1$ boundaries (Fig. 7). The sensitivity of the model to these parameters is analogous to the sensitivity observed with the spring-and-slider system (Fig. 1). The same four domains are observed depending on whether sliding is stick-slip ($\kappa_c > 1$) or stable ($\kappa_c < 1$), and on whether inertial vibrations are excited ($\eta > 1$) or not ($\eta < 1$) (Figs. 7 and 8). For example, the simulations corresponding to Figs. 8a and 8b, in the domain where $\kappa_c > 1$ and $\eta < 1$, show clearly a stick-slip behavior and no visible inertial vibrations. Inertial vibrations are excited if the effective normal stress is low enough or the velocity is high enough to yield $\eta > 1$, as happened in the simulations corresponding to Figs. 8f, 8h, and 8i. Fig. 8h confirms that temporal inertial vibration can emerge with moderate velocity perturbation if normal stress is low enough even if $\kappa_c < 1$. So $\kappa_c > 1$ is not a strict requirement for inertial vibrations.

Despite the general similarity, we observe a substantial difference between the boundary elements and the spring-and-slider simulations. In the case of $\kappa_c > 1$ and $\eta \gg 1$, the amplitude of

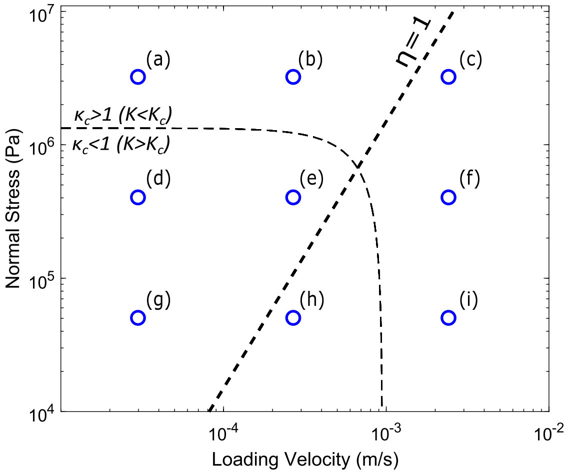

Fig. 7. Loading velocity and normal stress in the lumped-mass boundary element simulations of Fig. 8 with the contour of $\kappa_c = 1$ and $\eta = 1$ assuming shape factor $\alpha = 1$. The simulations are labeled according to the panels of Fig. 8. We used definition of $\kappa_c = 1$ and $\eta = 1$ defined at spring slider system (i.e., equation (4) and (7)) with equivalent K (equation (12)) and input parameter $M = 450000$ kg/m^2 (which is calculated based on equation (21)). Simulation results with higher velocities are presented in figure S4.

the vibration attenuates with time (Fig. 8i) while it is stationary in the spring-and-slider simulation (Fig. 1j). The attenuation in the boundary elements simulations seems associated with the development of multi-mode vibrations. Since the mechanical energy of a wave is proportional to (frequency × amplitude)^2, higher mode (i.e., higher frequency) vibration should have a lower amplitude at the same energy radiation rate. The amplitude attenuation at higher mode can be observed in our fully dynamic simulations (e.g., Figs. 6b&c, figure S16). When the loading velocity is increased further, the simulations yield multi-mode vibrations (figure S4b) or faster-attenuating vibrations (figure S4c&d). We indeed observe a larger contribution of high-frequency components for the simulation with a higher loading rate (figure S5 blue). We hypothesize that the attenuation results from a transfer of energy from the fundamental mode to higher modes.

The dominant frequency of the inertial vibration is very close of the expected value of 1.5 Hz (figure S5) estimated from equation (9). We indeed obtain 1.5 Hz for $G = 30$ Gpa, $\nu = 0.25$, $L = 1$ km and assuming $\alpha = 1$, given that the lumped stiffness is $K = 40$ MPa/m (equation (12)), and lumped mass $M = 450000$ kg/m^2 (equation (21)).

4.2.2. Joint simulation of slow slip and inertial vibrations

Fig. 9 shows that, as expected, our set-up results in spontaneous slow slip events and inertial vibrations radiated by the patch with locally low effective normal stress. The chosen model parameters result in slip events with ∼100 days recurrence interval. Interestingly, two different types of events are alternating (Fig. 9a).

Type (i) events are associated with tremor (at ∼180, ∼380 day), and type (ii) events are not (at ∼80, ∼280 day). Both types nucleate at the stable/unstable boundary (2, 8 km) and propagate toward the center (Fig. 9). The inward propagating slow slip events propagate at a velocity of ∼10-20 km/day (Fig. 9b). The slip rate is of the order of a few micrometers per second. During type (ii) events, slow slip fades out before reaching the central patch (Fig. 9c). By contrast, slow slip during type (i) events reaches the center inducing inertial vibration of the central patch of low normal stress and a re-rupture of the fault by a pulse of slow-slip, which propagates outward, away from the resonating central patch (Fig. 9b).

A strong inertial vibration is associated with the slow slip at the central low normal stress anomaly (Fig. 10). The vibration is initiated at the beginning of the velocity increase and attenuates with time. Considering that the vibration patch size (400 m) and assigned M (180000 kg/m^3) are smaller than that of Fig. 8 simulations (1 km and 450000 kg/m^3), the system is in the attenuating tremor zone ($\kappa_c < 1$ and $\eta > 1$) since sustained vibration ($\kappa_c > 1$ and $\eta > 1$) requires larger velocity than the simulated slip rate (< 100 μm/s). This shows that $\kappa_c > 1$ is not required, but the tremor can emerge whenever normal stress is low enough.

5. Discussion

Our study shows that inertial vibrations can be excited by slow slip events. In the case of a single-degree-of-freedom spring-and-slider system, the inertial vibrations can be excited by frictional sliding if $\eta = MV^2/\sigma' aD_c \gg 1$. We recall that this condition is only approximative and not derived from a rigorous stability analysis. Note that the instability condition ($\kappa_c > 1$) is not required since inertial vibrations can still emerge but would attenuate with time (Fig. 1). Therefore, the potential for inertial vibration is enhanced when the loading rate, V_l, is temporarily increased and effective normal stress σ' is low. These two conditions could be met on a fault patch with high pore pressure during slow slip events. Our model thus provides a possible explanation of tectonic tremors associated with slow slip events in subduction zone settings or on continental faults.

Tremor emergence in 1-D fault is primarily controlled by σ' and V_l, but the sensitivity to fault size L is less straightforward to assess. The mass of the equivalent lumped-mass simulation is linearly dependent on the length L of the resonating patch. Hence, an increase in L in 1D fault would increase M and accordingly increases η. One may consider that a large-size fault would then be more prone to inertial vibrations. However, an increase in L also decreases the stiffness of the system, which also influences vibration emergence (Im et al., 2019). Note that the inertial number for the 1-D fault, q (equation (11)), depends on the density but is independent of the fault length.

The slip rate and propagation rate in our simulation of ETS are of the same order of magnitude as those associated with large slow slip events in Cascadia (e.g., Bartlow et al., 2011). The outward propagating slow slip events that are generated together with the tremor-like vibrations during type (i) events propagate initially much faster at a rate of >800 km/day (Fig. 10a). This feature is reminiscent of the rapid tremor reversals observed in Cascadia (Houston et al., 2011). A proper exploration of that analogy would require 2-D simulations and is beyond the scope of this study.

The natural frequency of a fault patch is dependent on its length and the shear modulus G, and rock density ρ (equation (20)). Accordingly, for values typical of rocks, such as the values of $G = 30$ GPa and $\rho = 2400$ kg chosen in our simulations, the 1-10 Hz frequency range of tremor in ETS events (e.g., Beroza and Ide, 2011) corresponds to a fault length of 170 to 1700 m. It should be noted that the duration of slow-slip events in our simulations of ETS is much shorter than slow slip events in Cascadia due to the small size of the fault generating the slow slip events that were chosen to limit the computational cost.

Our model can inherently explain the long-duration non-impulsive nature of tremor and requires only two conditions, first a mechanism allowing for transient aseismic slip and second the existence of fault patches with near lithostatic pore pressure – for the emergence of tremor during slow slip events. Regarding the generation of slow events, we have assumed a friction law with a transition from rate-weakening to rate-strengthening at a higher slip rate. Other mechanisms have been proposed and could also be combined with our mechanism of tremor generation as inertial vi-

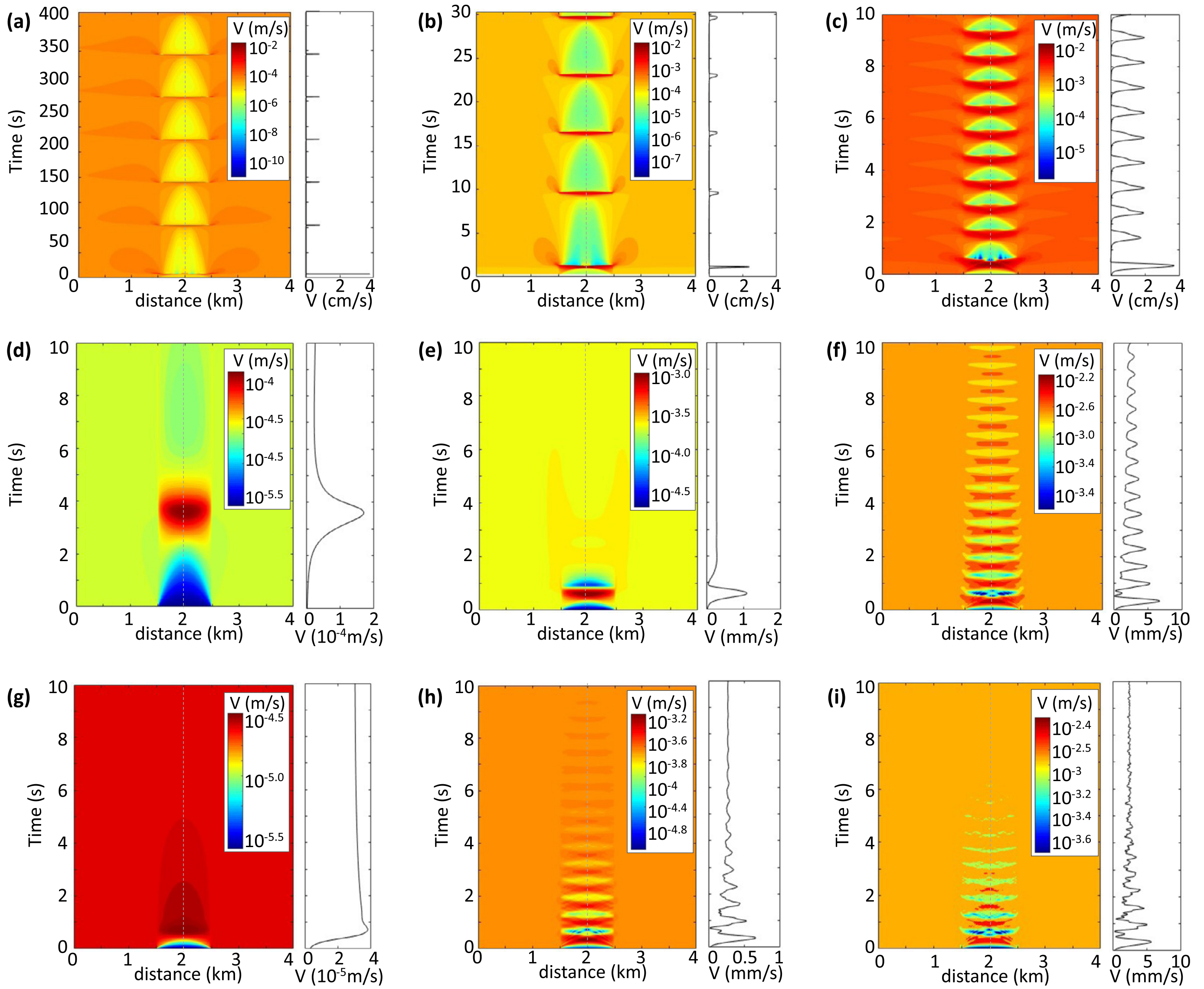

Fig. 8. Lumped mass boundary element simulation results of time-dependent velocity change. Velocity at the center of the unstable zone (dashed line) is separately plotted on the right side. Loading velocity and normal stresses in each case are shown in Fig. 7. See Fig. 2c for input parameter distributions.

brations. They include, for example, dilatant strengthening (Segall et al., 2010), mixed brittle and viscous rheological properties (Skarbek et al., 2012; Lavier et al., 2021), and pressure wave migration in an anisotropic viscoplastic shear zone (Yin, 2018). Most importantly, our model requires the presence of patches of low effective normal stress within the zone of transient slip. The fact that fluids are released by metamorphic reactions during subduction and the natural self-affine roughness of faults (e.g., Brodsky et al., 2016), seafloor irregularities due to seamounts and fractures, and lithological heterogeneities (Behr et al., 2018) could be the reason for the existence of such patches along with the subduction interface. Our analysis implies quasi-harmonic vibrations in the case of a single patch of a given size, but heterogeneities in nature would imply fault patches of various sizes scattered within the ETS zone. Once the loading rate is perturbed by slow slip, the various patches with low effective normal stress zone would vibrate at different resonance frequencies. Therefore, the collective tremor signal detected at the surface would not be a single harmonic signal but could span a broad range of frequencies, as observed in tectonic tremor (e.g., Shelly et al., 2007; Schwartz and Rokosky, 2007).

We note that our model does not conflict with the existing view of tremor as a swarm of low-frequency earthquakes (Shelly et al., 2007). This view was also tested using numerical simulations, which considered seismogenic patches embedded within stable surroundings (Ando et al., 2012; Luo and Ampuero, 2018; Luo and Liu, 2019). In our simulation, the tremor emergence is only localized within the high-pressure patch (Fig. 10). Conversely, in the non-tremorgenic surrounding area, the initial ($<$ 100 s) slip motion can be viewed as a (very) low-frequency earthquake (LFE), which propagates as a slow slip at the later stage (Figs. 9 and 10). If low-normal-stress zones are scattered within the slow slip zone due to the heterogeneity of fault asperity, ETS can also be understood as a swarm of these partly tremor-like, partly LFE-like events that eventually evolve toward slow slip. Our model thus provides an integrated view of slow slip, LFE, and tremor and shows that they are interdependent within ETS events as observed in natural examples (Ghosh et al., 2015).

Our tremor model differs from the model of Dmitrieva et al. (2013), which assumes a high-frequency stick-slip behavior forced by a high slip rate observed in simulations with a quasi-dynamic approximation. As we show in section 2.2, the quasi-dynamic ap-

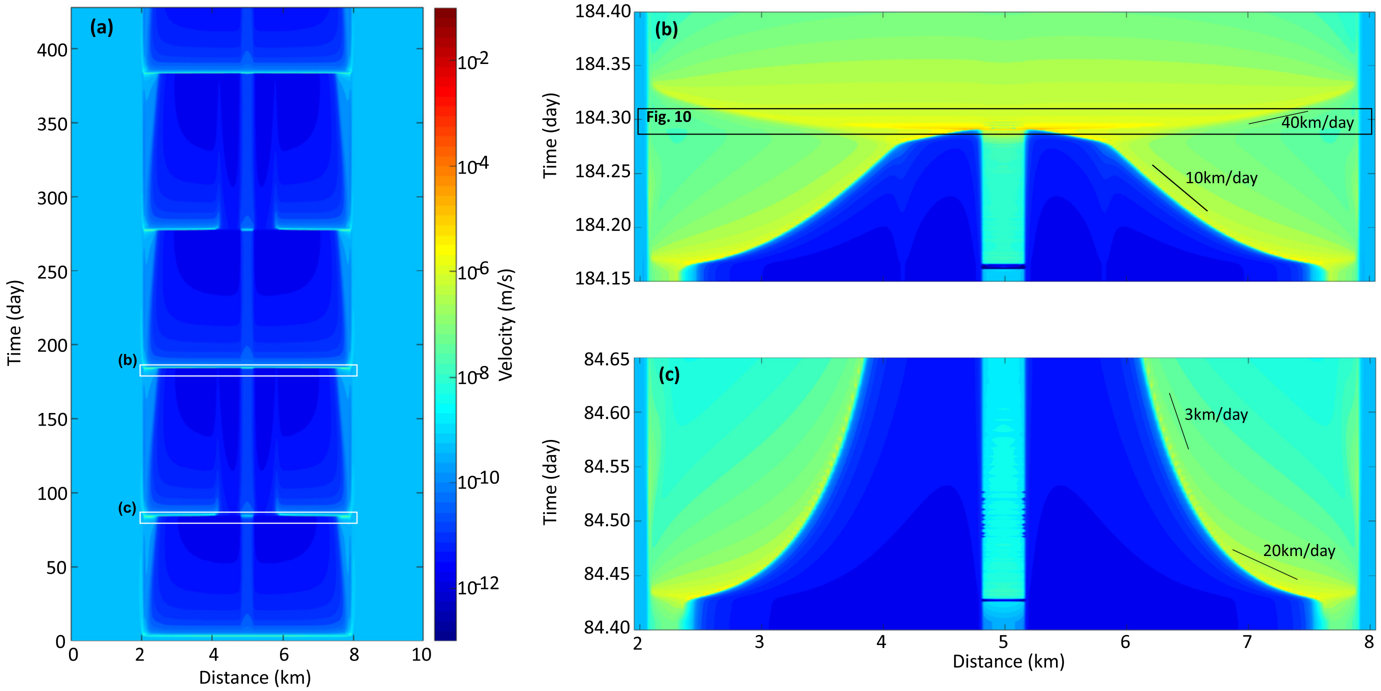

Fig. 9. Simulation of slow slip events in the case of a central patch with low effective normal stress. (a) Slip-rate with time. (b,c) zoomed-in view of the two types of slow slip events (type (i) at time ∼180 day (b), type (ii) at time ∼80 day (c)). Type (i) events are associated with inertial vibrations of the central patch (Fig. 10), but type (ii) events fail to reach the center part of the fault and don't excite inertial vibrations.

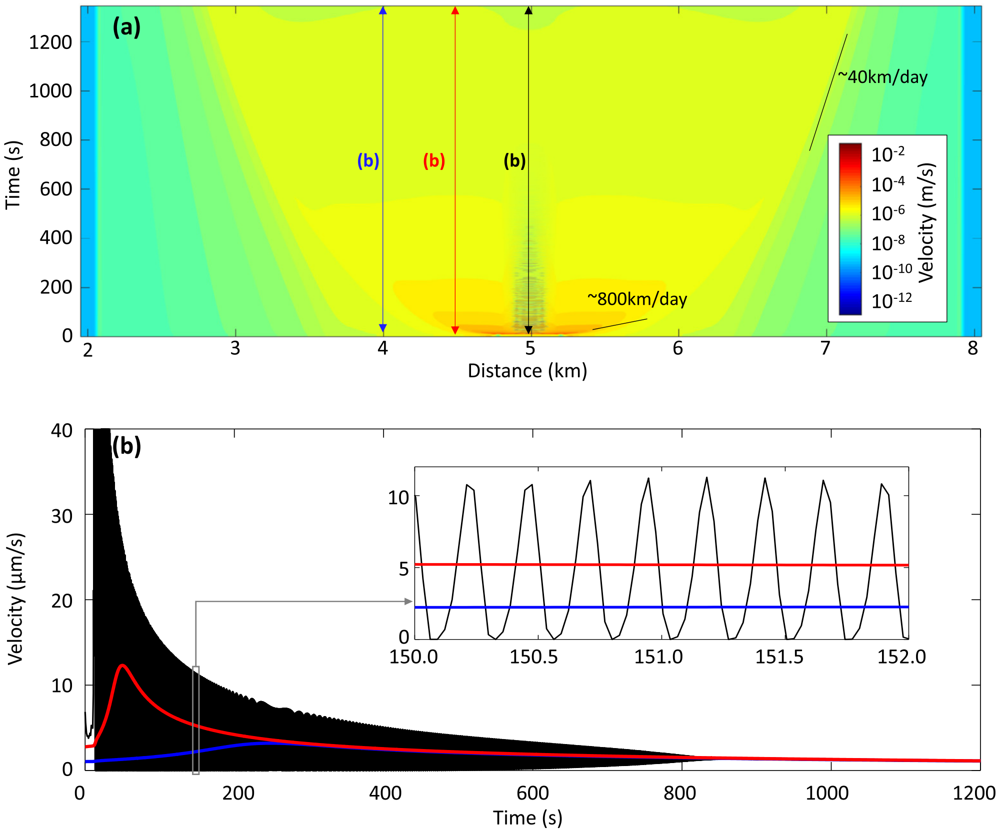

Fig. 10. (a) Zoom-in view of the resonance of the central patch during a type (i) event and the reverse propagation of slow slip (see the box in panel b of Fig. 9). (b) Velocity profile at the location denoted in panel a. The angularness of the curve in the inset is due to the simulation sampling rate. See Fig. 2d for input parameter distributions.

proximation might not be valid for the high slip rate associated with 1-10 Hz frequency unstable slip motion. Stick-slip motion consists of alternating short slip-phases and longer stick-phases. As the loading rate increases, the frequency of slip-events increases because the duration of the stick phase decreases. However, the reduction of the slip-phase duration is limited by inertia. As the loading rate increases, the duration of the stick-phase reduces, and finally, the motion is dominated by the slip-phase, making it a high-frequency oscillation of acceleration and deceleration, i.e., inertial vibration.

In the spring-and-slider system, the frequency is strictly limited to its natural frequency, but this restriction is less strict in the 1D fault model. Fig. 5 shows higher modes excitation at high velocity. Moreover, even before the higher mode excitation, the frequency still continuously increases with the velocity at a given fault length. This velocity-dependent frequency drift might partly explain the continuous gliding observed in the volcanic tremor (e.g., Dmitrieva et al., 2013; Hotovec et al., 2013; MacAyeal et al., 2008). However, the observed gliding tremor does not seem to have the higher mode excitation observed in our simulations. As it stands, our model may not explain the strong continuous gliding. However, it is likely that inertia is still essential to explain such high-frequency vibrations.

6. Conclusion

Our model shows that inertial vibrations can be excited by slow fault slip and that this mechanism could be the cause of tectonic tremor. The model is consistent with the characteristics of tremors associated with slow slip events at subduction zones. The model might also apply to volcanic tremors since it might also be associated with fault slip (e.g., Dmitrieva et al., 2013).

CRediT authorship contribution statement

Kyungjae Im: Conceptualization, Methodology, Software, Writing – original draft. **Jean-Philippe Avouac:** Conceptualization, Validation, Writing – review & editing.

Declaration of competing interest

The authors declare that they have no known competing financial interests or personal relationships that could have appeared to influence the work reported in this paper.

Acknowledgement

We thank two anonymous reviewers for their insightful and constructive evaluations and Jean-Paul Ampuero for valuable discussions. This study was supported by NSF EAR-1821853.

Appendix A. Supplementary material

Supplementary material related to this article can be found online at https://doi.org/10.1016/j.epsl.2021.117238.

References

Ando, R., Takeda, N., Yamashita, T., 2012. Propagation dynamics of seismic and aseismic slip governed by fault heterogeneity and Newtonian rheology. J. Geophys. Res., Solid Earth 117 (B11). https://doi.org/10.1029/2012JB009532.

Audet, P., Schaeffer, A.J., 2018. Fluid pressure and shear zone development over the locked to slow slip region in Cascadia. Sci. Adv. 4 (3). https://doi.org/10.1126/sciadv.aar2982.

Bartlow, N.M., Miyazaki, S., Bradley, A.M., Segall, P., 2011. Space-time correlation of slip and tremor during the 2009 Cascadia slow slip event. Geophys. Res. Lett. 38 (18). https://doi.org/10.1029/2011GL048714.

Baumberger, T., Caroli, C., 2006. Solid friction from stick-slip down to pinning and aging. Adv. Phys. 55 (3–4), 279–348. https://doi.org/10.1080/00018730600732186.

Behr, W.M., Kotowski, A.J., Ashley, K.T., 2018. Dehydration-induced rheological heterogeneity and the deep tremor source in warm subduction zones. Geology 46 (5), 475–478. https://doi.org/10.1130/G40105.1.

Beroza, G.C., Ide, S., 2011. Slow earthquakes and nonvolcanic tremor. Annu. Rev. Earth Planet. Sci. 39 (1), 271–296. https://doi.org/10.1146/annurev-earth-040809-152531.

Bhattacharya, P., Rubin, A.M., Bayart, E., Savage, H.M., Marone, C., 2015. Critical evaluation of state evolution laws in rate and state friction: fitting large velocity steps in simulated fault gouge with time-, slip-, and stress-dependent constitutive laws. J. Geophys. Res., Solid Earth 120 (9), 6365–6385. https://doi.org/10.1002/2015JB012437.

Brodsky, E.E., Kirkpatrick, J.D., Candela, T., 2016. Constraints from fault roughness on the scale-dependent strength of rocks. Geology 44 (1), 19–22. https://doi.org/10.1130/G37206.1.

Brown, K.M., Tryon, M.D., DeShon, H.R., Dorman, L.M., Schwartz, S.Y., 2005. Correlated transient fluid pulsing and seismic tremor in the Costa Rica subduction zone. Earth Planet. Sci. Lett. 238 (1), 189–203. https://doi.org/10.1016/j.epsl.2005.06.055.

Calvert, A.J., Bostock, M.G., Savard, G., Unsworth, M.J., 2020. Cascadia low frequency earthquakes at the base of an overpressured subduction shear zone. Nat. Commun. 11 (1), 3874. https://doi.org/10.1038/s41467-020-17609-3.

Chouet, B.A., Matoza, R.S., 2013. A multi-decadal view of seismic methods for detecting precursors of magma movement and eruption. J. Volcanol. Geotherm. Res. 252, 108–175. https://doi.org/10.1016/j.jvolgeores.2012.11.013.

Crouch, S.L., 1976. Solution of plane elasticity problems by the displacement discontinuity method. I. Infinite body solution. Int. J. Numer. Methods Biomed. Eng. 10 (2), 301–343. https://doi.org/10.1002/nme.1620100206.

Dieterich, J.H., 1979. Modeling of rock friction: 1. Experimental results and constitutive equations. J. Geophys. Res. 84 (9), 2161–2168.

Dieterich, J.H., 1992. Earthquake nucleation on faults with rate-and state-dependent strength. Tectonophysics 211 (1), 115–134. https://doi.org/10.1016/0040-1951(92)90055-B.

Dieterich, J.H., Kilgore, B.D., 1994. Direct observation of frictional contacts: new insights for state-dependent properties. Pure Appl. Geophys. 143 (1–3), 283–302. https://doi.org/10.1007/BF00874332.

Dmitrieva, K., Hotovec-Ellis, A.J., Prejean, S., Dunham, E.M., 2013. Frictional-faulting model for harmonic tremor before Redoubt Volcano eruptions. Nat. Geosci. 6 (8), 652–656. https://doi.org/10.1038/ngeo1879.

Ghosh, A., Huesca-Pérez, E., Brodsky, E., Ito, Y., 2015. Very low frequency earthquakes in Cascadia migrate with tremor. Geophys. Res. Lett. 42 (9), 3228–3232. https://doi.org/10.1002/2015GL063286.

Hawthorne, J.C., Rubin, A.M., 2010. Tidal modulation of slow slip in Cascadia. J. Geophys. Res., Solid Earth 115 (B9). https://doi.org/10.1029/2010JB007502.

Houston, H., Delbridge, B.G., Wech, A.G., Creager, K.C., 2011. Rapid tremor reversals in Cascadia generated by a weakened plate interface. Nat. Geosci. 4 (6), 404–409. https://doi.org/10.1038/ngeo1157.

Hotovec, A.J., Prejean, S.G., Vidale, J.E., Gomberg, J., 2013. Strongly gliding harmonic tremor during the 2009 eruption of Redoubt Volcano. J. Volcanol. Geotherm. Res. 259, 89–99. https://doi.org/10.1016/j.jvolgeores.2012.01.001.

Ibrahim, R.A., 1994. Friction-induced vibration, chatter, squeal, and chaos Part I: mechanics of contact and friction. Appl. Mech. Rev. 47, 209–226.

Itasca Consulting Group, Inc., 2007. FLAC3D — Fast Lagrangian Analysis of Continua in Three-Dimensions. Ver. 4.0, Itasca, Minneapolis.

Im, K., Elsworth, D., Marone, C., Leeman, J., 2017. The impact of frictional healing on stick-slip recurrence interval and stress drop: implications for earthquake scaling. J. Geophys. Res., Solid Earth. https://doi.org/10.1002/2017JB014476.

Im, K., Marone, C., Elsworth, D., 2019. The transition from steady frictional sliding to inertia-dominated instability with rate and state friction. J. Mech. Phys. Solids. https://doi.org/10.1016/j.jmps.2018.08.026.

Im, K., Saffer, D., Marone, C., Avouac, J.-P., 2020. Slip-rate-dependent friction as a universal mechanism for slow slip events. Nat. Geosci. 13 (10), 705–710. https://doi.org/10.1038/s41561-020-0627-9.

Julian, B.R., 1994. Volcanic tremor: nonlinear excitation by fluid flow. J. Geophys. Res., Solid Earth 99 (B6), 11859–11877. https://doi.org/10.1029/93JB03129.

Kinkaid, N.M., O'Reilly, O.M., Papadopoulos, P., 2003. Automotive disc brake squeal. J. Sound Vib. 267 (1), 105–166. https://doi.org/10.1016/S0022-460X(02)01573-0.

Lapusta, N., Rice, J.R., Ben-Zion, Y., Zheng, G., 2000. Elastodynamic analysis for slow tectonic loading with spontaneous rupture episodes on faults with rate- and state-dependent friction. J. Geophys. Res. 105, 23765. https://doi.org/10.1029/2000JB900250.

Lavier, L.L., Tong, X., Biemiller, J., 2021. The mechanics of creep, slow slip events, and earthquakes in mixed Brittle-Ductile fault zones. J. Geophys. Res., Solid Earth 126 (2), e2020JB020325. https://doi.org/10.1029/2020JB020325.

Luo, Y., Ampuero, J.-P., 2018. Stability of faults with heterogeneous friction properties and effective normal stress. Tectonophysics 733, 257–272. https://doi.org/10.1016/j.tecto.2017.11.006.

Luo, Y., Liu, Z., 2019. Rate-and-state model casts new insight into episodic tremor and slow-slip variability in Cascadia. Geophys. Res. Lett. 46 (12), 6352–6362. https://doi.org/10.1029/2019GL082694.

MacAyeal, D.R., Okal, E.A., Aster, R.C., Bassis, J.N., 2008. Seismic and hydroacoustic tremor generated by colliding icebergs. J. Geophys. Res., Earth Surf. 113 (F3).

Marone, C., 1998. Laboratory-defived friction laws and their application to seismic faulting. Annu. Rev. Earth Planet. Sci. 26 (1), 643–696. https://doi.org/10.1146/annurev.earth.26.1.643.

Miller, M.M., Melbourne, T., Johnson, D.J., Sumner, W.Q., 2002. Periodic slow earthquakes from the Cascadia subduction zone. Science 295 (5564), 2423. https://doi.org/10.1126/science.1071193.

Nadeau, R.M., Dolenc, D., 2005. Nonvolcanic tremors deep beneath the San Andreas fault. Science 307 (5708), 389. https://doi.org/10.1126/science.1107142.

Obara, K., 2002. Nonvolcanic deep tremor associated with subduction in southwest Japan. Science 296 (5573), 1679–1681. https://doi.org/10.1126/science.1070378.

Rabinowitz, H.S., Savage, H.M., Skarbek, R.M., Ikari, M.J., Carpenter, B.M., Collettini, C., 2018. Frictional behavior of input sediments to the Hikurangi Trench, New Zealand. Geochem. Geophys. Geosyst. 19, 2973–2990. https://doi.org/10.1029/2018GC007633.

Rice, J.R., 1993. Spatio-temporal complexity of slip on a fault. J. Geophys. Res. 98 (B6), 9885. https://doi.org/10.1029/93JB00191.

Rice, J.R., Ruina, A.L., 1983. Stability of steady frictional slipping. J. Appl. Mech. 50 (2), 343. https://doi.org/10.1115/1.3167042.

Rice, J.R., Lapusta, N., Ranjith, K., 2001. Rate and state dependent friction and the stability of sliding between elastically deformable solids. J. Mech. Phys. Solids 49 (9), 1865–1898. https://doi.org/10.1016/S0022-5096(01)00042-4.

Rice, J.R., Tse, S.T., 1986. Dynamic motion of a single degree of freedom system following a rate and state dependent friction law. J. Geophys. Res. 91 (1), 521–530.

Rogers, G., Dragert, H., 2003. Episodic tremor and slip on the Cascadia subduction zone: the chatter of silent slip. Science 300 (5627), 1942–1943. https://doi.org/10.1126/science.1084783.

Rousset, B., Bürgmann, R., Campillo, M., 2019. Slow slip events in the roots of the San Andreas fault. Sci. Adv. 5 (2). https://doi.org/10.1126/sciadv.aav3274.

Rubinstein, J.L., La Rocca, M., Vidale, J.E., Creager, K.C., Wech, A.G., 2008. Tidal modulation of nonvolcanic tremor. Science 319 (5860), 186–189. https://doi.org/10.1126/science.1150558.

Ruina, A., 1983. Slip instability and state variable friction laws. J. Geophys. Res. 88, 10359–10370.

Schwartz, S.Y., Rokosky, J.M., 2007. Slow slip events and seismic tremor at Circum-Pacific subduction zones. Rev. Geophys. 45 (3). https://doi.org/10.1029/2006RG000208.

Segall, P., Rubin, A.M., Bradley, A.M., Rice, J.R., 2010. Dilatant strengthening as a mechanism for slow slip events. J. Geophys. Res., Solid Earth 115 (B12). https://doi.org/10.1029/2010JB007449.

Shelly, D.R., 2010. Migrating tremors illuminate complex deformation beneath the seismogenic San Andreas fault. Nature 463 (7281), 648–652. https://doi.org/10.1038/nature08755.

Shelly, D.R., Beroza, G.C., Ide, S., 2007. Non-volcanic tremor and low-frequency earthquake swarms. Nature 446 (7133), 305–307. https://doi.org/10.1038/nature05666.

Shelly, D.R., Beroza, G.C., Ide, S., Nakamula, S., 2006. Low-frequency earthquakes in Shikoku, Japan, and their relationship to episodic tremor and slip. Nature 442, 188–191. https://doi.org/10.1038/nature04931.

Skarbek, R.M., Rempel, A.W., Schmidt, D.A., 2012. Geologic heterogeneity can produce aseismic slip transients. Geophys. Res. Lett. 39 (21). https://doi.org/10.1029/2012GL053762.

Smith, J.H., Woodhouse, J., 2000. The tribology of rosin. J. Mech. Phys. Solids 48 (8), 1633–1681. https://doi.org/10.1016/S0022-5096(99)00067-8.

Thomas, A.M., Bürgmann, R., Shelly, D.R., Beeler, N.M., Rudolph, M.L., 2012. Tidal triggering of low frequency earthquakes near Parkfield, California: implications for fault mechanics within the brittle-ductile transition. J. Geophys. Res., Solid Earth 117 (B5). https://doi.org/10.1029/2011JB009036.

Yin, A., 2018. Water hammers tremors during plate convergence. Geology 46 (12), 1031–1034. https://doi.org/10.1130/G45261.1.